City Research Online

City, University of London Institutional Repository

Citation: Elshalakani, M. & Brücker, C. (2020). Simulation of self-coordination in a row of beating flexible flaplets for micro-swimmer applications: Model and experiment study. Journal of Fluids and Structures, 94, 102923. doi: 10.1016/j.jfluidstructs.2020.102923

This is the accepted version of the paper.

This version of the publication may differ from the final published version.

Permanent repository link: https://openaccess.city.ac.uk/id/eprint/24158/

Link to published version: https://doi.org/10.1016/j.jfluidstructs.2020.102923

Copyright: City Research Online aims to make research outputs of City, University of London available to a wider audience. Copyright and Moral Rights remain with the author(s) and/or copyright holders. URLs from City Research Online may be freely distributed and linked to.

Reuse: Copies of full items can be used for personal research or study, educational, or not-for-profit purposes without prior permission or charge. Provided that the authors, title and full bibliographic details are credited, a hyperlink and/or URL is given for the original metadata page and the content is not changed in any way.

City Research Online: http://openaccess.city.ac.uk/ publications@city.ac.uk

Highlights

Simulation of Self-Coordination in a Row of Beating Flexible Flaplets for Micro-Swimmer Applications: Model and Experiment Study

Mohamed Elshalakani,Christoph Bruecker

- Modelling of a row of oscillating cilia-like structures
- Presentation of the spontaneous emergence of metachronal coordination
- Validation of the model design and results experimentally
- Study of the effective propulsion that results from the coordination

Simulation of Self-Coordination in a Row of Beating Flexible Flaplets for Micro-Swimmer Applications: Model and Experiment Study

Mohamed Elshalakani[a,*], Christoph Bruecker[a]

[a] *Department of Mechanical Engineering and Aeronautics, City University of London, Northampton Square, London EC1V 0HB, UK*

ARTICLE INFO

Keywords:
Process modelling and control
Self-assembly
Fluid-structure interaction
Micro-swimmers

ABSTRACT

In this study we present a model that simulates hydrodynamic self-coordination in a row of flexible flaplets. We control the flaplets in order that their tips follow a fixed-amplitude oscillatory motion profile. When brought together at a low Reynolds-number environment, the flaplets interact with each other in the form of bending deflections at their tips, which causes the frequency of the individual oscillations to vary until a coordinated steady state is reached. The model design steps are experimentally verified and the coordination results of both the experiment and the model are compared. The model's internal states are then analysed for a better understanding of the synchronization collective effect. The coordination of the flaplets is found to settle in the direction of propulsion forces ascent. The stability of the resulted synchronization and propulsion forces are examined over long periods. The model is meant to be simplified and mostly linear so that it can be utilized for state forecasting in a real-time control application of a swimmer robot. Finally, we experimentally study the propulsion performance of five beating flaplets that follow prescribed oscillation profiles forming a metachronal wave. The flow results show that the flaplets, that beat in coordination, are efficient at generating a uni-directional steady-streaming transport of the fluid at their surface.

1. Introduction

Nature is full of examples where a collaborative behaviour rises due to different body reactions and surrounding environmental properties [9], [2], [3]. One of these examples is the hydrodynamic coordination of flagella and cilia in biology. Sperms while swimming interact with the surrounding semen and with each other forming a kind of cluster [51].In human windpipes, cilia beat in a coordinated pattern while sweeping away mucus and dirt outside of the lungs [45]. Similar coordination of cilia is witnessed at the surface of many ciliated organisms [43, 34, 46]. Each cilium is found to maintain a certain phase shift to its neighbours while beating forming a pattern that is known as a metachronal wave [21]. It is believed that when brought together, cilia are coupled by the surrounding fluid's viscous forces and over time they appear to organize their oscillations allowing that collective state to spontaneously emerge [24, 12, 13, 37, 46]. Previous numerical models and experiments have shown that hydrodynamic forces can bring different types of oscillators that are close to each other to various forms of self-organization [37, 19, 20, 32, 16, 41], even with breaks in their steady-state phase relationships [37, 19].

In the world of ciliated micro-swimmers, the viscous forces are dominant and fluid propulsion cannot be created by a time-symmetric oscillator as explained by the scallop theorem [40]. Consequently, most of the developed swimmer models or designs at low Reynolds numbers adopt the actuation of non-reciprocal motion profiles. Some examples of these designs are swimmers made of; (1) asymmetric rod joints [8] (2) soft deformable interfaces [35, 47] (3) connected spheres with certain kinematic interrelations [18, 17, 36]. (4) helical vibrating interfaces [22, 50]. In such non-reciprocal motion profiles, the asymmetry of the generated viscous forces induce a net propulsion force in a certain direction [29, 1]. However, when a model of artificial cilia, that can be magnetically actuated to follow non-reciprocal beating profiles, was examined in [23], it was shown that the pumping performance of interacting coordinated cilia was significantly higher than that of separate ones. Similarly, in [11, 13], it is stated that the coordinated beating of cilia is particularity effective at maintaining a more directed surface propulsion. It has been also shown that the propulsive effect of a system of pneumatically controlled flexible oscillators is strongly affected by their phase relationships [44]. Accordingly, we suggest that the metachronal coordination of a system of individual oscillators can result in collective propulsion if the oscillators are brought together in a sufficiently-viscous environment.

Generally, further progression to realistic micro-swimmer robotic applications faces two main challenges; (1) the design and control of applicable propulsion mechanisms and (2) the minimization of the actuation power [14]. In case of using oscillating elements to generate propulsion, a minimum of two degrees of freedom per each element is required to be controlled to satisfy the desired non-reciprocal motion profiles [29]. In some models, even the shape of the elements is required to be changed during different parts of the beating cycle which brings more complexity to the system and control [23]. Additionally, most of the micro-swimmer models are usually developed using multi-particle collision dynamics (MPC) [28, 19] or other numerical solutions. Since, the computations of finite element models are time consuming, the real-time tracking of the robot's internal states using such models is not possible. Hence, we claim that swimmer de-

---

[*] Corresponding author

Mohamed.Elshalakani.2@city.ac.uk (M. Elshalakani); Christoph.Bruecker@city.ac.uk (C. Bruecker)

ORCID(s): 0000-0001-9521-2919 (M. Elshalakani); 0000-0001-9521-2919 (C. Bruecker)

signs with linearised and fast-computed models could facilitate better control and observation of such systems.

In this article, we firstly test the emergence of metachronal coordination in a row of flexible flaplets at a low Reynolds number by means of an experimentally-validated model. A single degree-of-freedom oscillatory motion is controlled by an algorithm that is based on the geometric clutch hypothesis [33] where the individual oscillations are bounded by amplitudes and free in phase and frequency. The induced bending of the flexible flaplets in the presence of a viscous medium allows for the crosstalk to take place within the beating system. The net swimming force that acts on the system is derived from the introduced model. The force analysis shows that the resulted synchronization can be accompanied with a net swimming effect. Then, the stability of the emerged synchronization is analysed over long periods showing that the emergence of synchronization can have a predictable steady-state behaviour. Finally, we experimentally visualize the flow field around the physical system using Particle Image Velocimetry (PIV) while the flaplets are beating in metachronal coordination. The measurement of the flow velocity field allows us to quantify the net pumping effect due to the coordinated beating of the flaplets.

2. Concept Formulation

2.1. Objective

We aim at studying the transformation of an oscillating system of beating flaplets from a chaotic to a coordinated pattern by means of an experimentally identified model. The key factors to get into coordination are the flexibility of the structures and the viscous coupling among them. A biological control hypothesis introduced by Lindemann [33] is implemented as the control algorithm, which follows the "geometric clutch". From there on, we look forward to highlight the collaborative swimming effect of the resulted coordination and study its stability.

2.2. Material and Environment

The proof-of-concept experiment of self-synchronization in a row of flexible flaplets were reported in detail in [20] and the reader is referred to it. Herein, the experiments are used to identify the parameters of the lumped element model of the flaplets. The physical problem of the bending of a thin flexible plate in a viscous environment is described by the two non-dimensional numbers, the Reynolds-number Re and the Cauchy number C_Y:

$$Re = \frac{U L_c}{\nu} \tag{1}$$

$$C_Y = \frac{\frac{1}{2}\rho U^2}{EI} \tag{2}$$

with ν being the fluid's kinematic viscosity, U the relative speed between the oscillator and the fluid, L_c the characteristic length in the problem geometry, EI the flexural rigidity and $\frac{1}{2}\rho U^2$ the dynamic pressure of the system. The Cauchy number characterizes the deformation of an elastic solid under the effect of a surrounding flow [15]. It is defined as the ratio between the force produced by the dynamic pressure of a flow on the flaplet surface and the bending rigidity of the rectangular flaplet.

The configuration under investigation herein is for a Re-number in the range of Re $\in [0.1, 1]$ and a Cauchy-number of order $C_Y = O(10^{-1})$. The method of dynamical similarity [7] enables us to use the results of an enlarged experimental model to investigate an observation that happens at a much smaller scale. It also enable us to use normalized quantities of size and speed in our theoretical model.

3. Experiment Description

3.1. Set-Up

Laboratory experiments were conducted with a row of five rectangular flaplets (thickness $t = 2$ mm, width $w = 20$ mm, length $l = 40$ mm) with an interspacing of b = 22 mm, inserted in a chamber filled with a sugar solution (100 % glycerine, $\mu = 0.95$ Pa·s), see Fig. 1. The row of flaplets represent the cilia-like structures in our experiment. In order to have optical access, all side-walls are made of transparent perspex. The flaplets are made of silicone rubber (density $\rho_f = 1.61\ g \cdot cm^{-3}$, Young's Modulus E = 6 MPa, see e.g. [49, 39]), which allows their for bending in response to the viscous coupling with their neighbours.

Each flaplet is inserted into a spindle axle of an individual motor that performs an oscillatory motion profile around its equilibrium position (where all oscillators are vertical), in which A is the tip motion amplitude prescribed for all of the individual flaplets and $\omega_0 = 0.267\ rad \cdot s^1$ is the angular speed. Without viscous coupling, all flaplets perform a fixed-amplitude triangular wave profile (symmetric forth-and-back tip motion) at constant period; $|\theta| \leq 0.22\, rad, T_c = 3.3\ s$. When the flaplets are inserted in the sugar-solution, the viscous coupling among the neighbouring oscillators cause the frequency of these oscillations to vary due to the bending of the flaplets. The amplitude of oscillations is selected so that the flaplets are not allowed to touch each others while beating. Therefore, a minimum distance, $r_{min} \simeq 0.2A$, between the tips is set at the nearest angular positions of a neighbouring couple of flaplets to allow for their bending deflections. We represent the distance r between the tips with an offset equal to the value of r_{min} so that; $r = 0$ when the tips are $|r_{min}|$ apart.

For optical detection, the tip of each flaplet is marked by a fluorescent marker, which is illuminated by a green LED light source and recorded with a high-speed camera (ProcImage 500-Eagle high-speed camera, $1280 \times 1024\ px^2$, Photon Lines Ltd, Bloxham, UK). By using an optical filter (cut-off wavelength 550 nm, Novasoft, Aarhus, Denmark) and adjusting the camera aperture, an image of only a row of dots, that correspond to the flaplet's tips, could be acquired, see Fig. 2. The positions of the dots are then tracked and their position is fed into the controller loop in real-time. Since the camera view is capturing the projection of the tip dis-

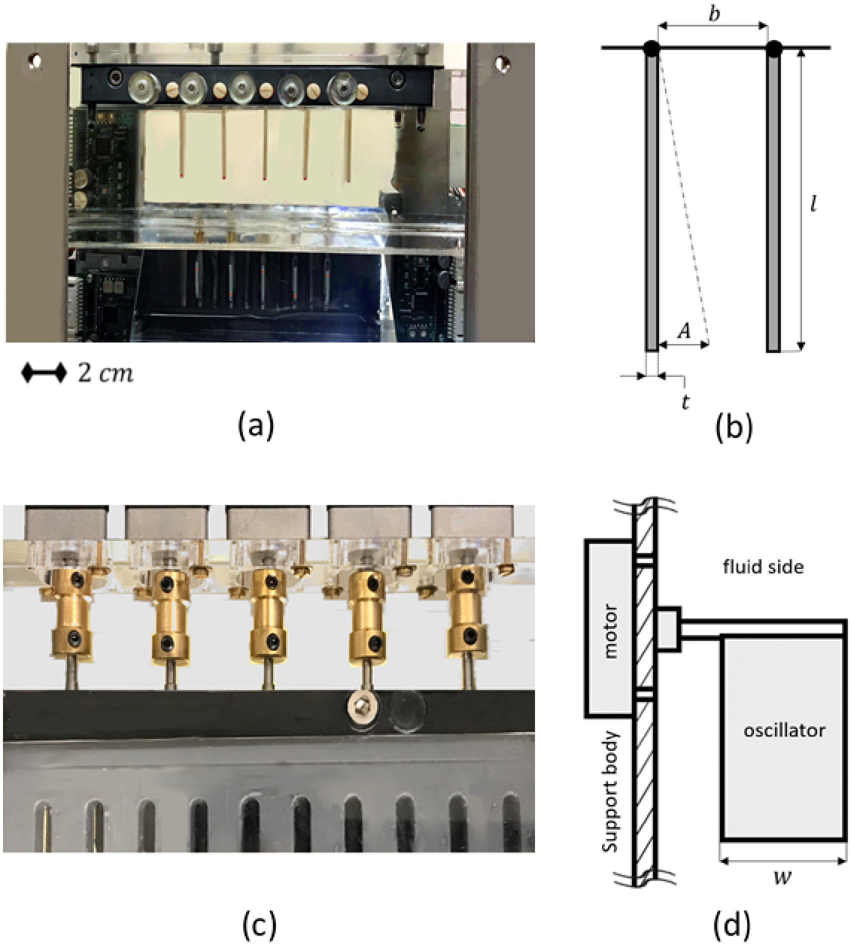

Figure 1: The experimental set-up of the five flexible flaplets in the viscous chamber. Each flaplet is clamped from one end to the spindle axle of a rotary motor. (a,b) front view (c) top view (d) side view (b,d) schematic drawings that show the geometrical parameters of the flaplets

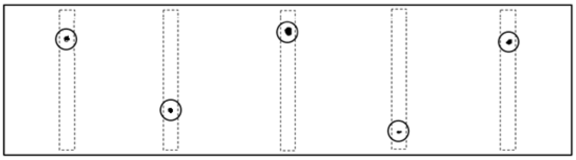

Figure 2: Acquired image of the flaplets' tips after binarization and colour inversion. For reference, circles and dash-lines are overlaid highlighting the dots and the tip contours respectively. The oscillatory motion is along the horizontal image axis, perpendicular to the flaplet span

placement in the camera plane, the triangular wave form is expected to be slightly distorted (displacement is captured as $r sin\theta$ instead of $r\theta$). However, at such small values of θ this distortion is fairly negligible.

3.2. Control Loop

Fig. 3 shows the implementation of the control loop in the experiment. The motion of the oscillators is controlled by a vision-based control algorithm. The acquired camera feed is sent on-line to the controller. Using the openCV library [38], a segmentation algorithm has been developed to obtain the coordinates of the individual flaplets in real-time. The controller detects the moment that each flaplet's tip reaches its predefined amplitude and toggles the direction of rotation of the attached motor. Alternatively, micro strain gauges can be used to measure value of deflection of the tips and trigger the reversal.

Fig. 4 shows the control algorithm that is applied to each oscillator. This logic is an implementation of the geometric clutch hypothesis that provides a geometrical mechanism of oscillations in biological swimmers [33]. To prove the unforced self-assembly of the flaplets, the motors are set to start rotating with random initial conditions forming a chaotic pattern. Since the oscillators are flexible, they bend due to the hydrodynamic forces that result from their own motion and the motion of their neighbouring oscillators. As a consequence of bending, the tip's position deviates from the locus of the tip of a rigid virtual oscillator at the same angle prescribed by the attached motor in that moment. With the given implementation of the clutch-hypothesis that tracks the locations of the oscillators' tips, the individual oscillations slightly vary in frequency during the runtime. This re-

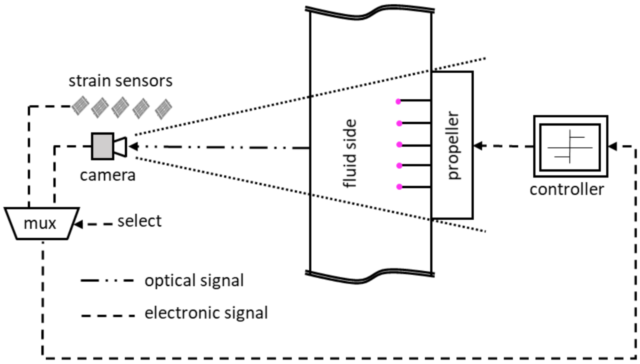

Figure 3: Physical implementation of the control closed-loop based on the geometric clutch hypothesis. The feedback signal is the position of the oscillators' tips that are marked with florescent dyes which can be captured by the high-speed camera. Another measurement of the feedback signal is applicable by the use of strain gauges that can capture the tips' deflection

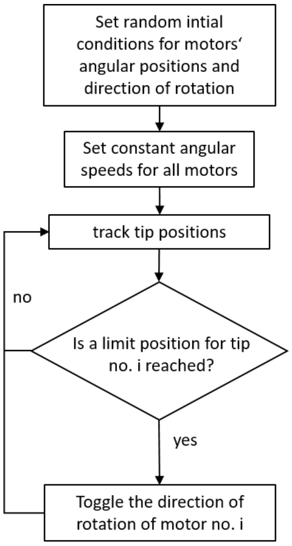
Set random intial conditions for motors' angular positions and direction of rotation
Set constant angular speeds for all motors
track tip positions
no
Is a limit position for tip no. i reached?
yes
Toggle the direction of rotation of motor no. i

Figure 4: Control algorithm of the individual oscillations

sults in a time-variant behaviour of the phase relationships among the oscillators which is essential for transforming the chaotic pattern of the system into a coordinated one. If the flaps were rigid, the viscous forces would not influence the phase relationships among the oscillators and hence they would keep their initial configuration prescribed at the beginning of the experiment.

4. Theoretical Modelling

We aim to introduce a simplified model of the experiment to study the synchronization behaviour for longer periods and larger number of flaplets. The fluid-structure interaction is approximated by a representation of the individual flaplets as flexible cantilever beams (Euler-Bernoulli beam) actuated by the individual motors and reacting to the surrounding pressure and viscous forces. The model is simplified and aligning with the experimental results. We expect that the simplicity of the model would be a significant advantage because, as elaborated later, the resulting coordination is found to be accompanied with the emergence of propulsion forces which qualifies the model for micro-swimmer applications. Hence, the observability and fastness would allow the model to be used for control design optimization and online state forecasting of swimmer robots in future applications.

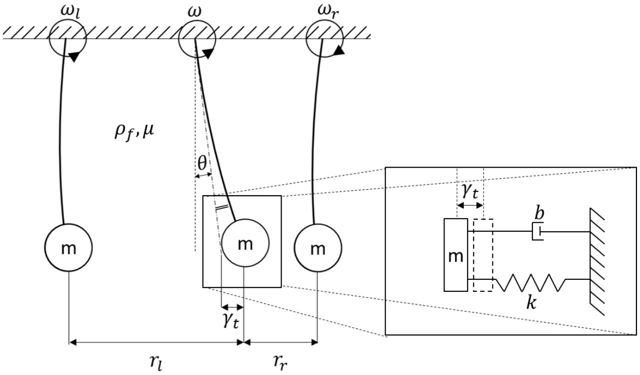

Figure 5: Lumped element model of the flaplet highlighting the viscous-coupling parameters. The description of the model parameters is provided in Table 1

4.1. Mathematical Description

In this section, we introduce the analytical equations that describe the behaviour of each oscillator while beating. Since the flaplets are identical, we can expand this model to describe a row of beating flaplets. The model equations are deduced and identified with the help of experimental and numerical data perceived from literature and tests in the experimental setup. The modelling design steps are comprehensively and experimentally validated. A detailed derivation of the mathematical model is provided in appendix A.

Table 1 and Fig. 5 illustrate the system parameters that come form the theoretical model of a single flaplet. The parameters are divide into the following four categories:

1. **Set Parameters**: these are the nominal constants that are given by the experimental setup and geometry.
2. **Input Variables**: these are the variables that are controlled by the operator or changed according to the states of the neighbouring flaplets. The flaplet perceives the inputs and responds accordingly in form of rotation and bending deflection.
3. **System States**: These form a set of variables that fully describe the flaplet at a given instance in time.
4. **Output Variables**: The response of the oscillator derived from the system states at a given instance.

In this case, we are particularly interested in the position trajectory of the flaplets's tip because the control loop uses this position as the feedback signal as illustrated in section 3.2. Before we start, we normalize all the system parameters against their nominal values to obtain a scalable dimensionless system of equations. The parameters of length units are

Table 1
Description of the parameters of the mathematical model

Symbol	Description	value
	Set Parameters	
ω_0 $[rad \cdot s^{-1}]$	angular speed of the attached motor	0.267
A $[m]$	limit amplitude of the tip position trajectory	9×10^{-3}
$T_c[s]$	nominal cycle period of the oscillatory motion	$4A/(\omega l)$
	Input Variables	
ω $[rad \cdot s^{-1}]$	angular velocity of the flaplet	$\pm\omega_0$
$\omega_{r,l}$ $[rad \cdot s^{-1}]$	angular velocity of the right/left neighbour	$\pm\omega_0$
$d_{r,l}$ $[-]$	relative angular velocity of the right/left neighbour normalized against ω_0	$(\omega_{r,l} - \omega)/\omega_0$
$r_{r,l}$ $[m]$	absolute distance from the oscillator's tip to the right/left neighbour's tip	
	System States	
θ $[rad]$	angular position of the straight oscillator (without accounting for the bending)	
γ_o $[m]$	deflection of the tip due to its rotation in the viscous liquid	
$\gamma_{r,l}$ $[m]$	deflection of the tip due to interaction with the right/ left neighbour neighbour	
γ_t $[m]$	total dynamic deflection at the oscillator's tip	
	Output Variables	
y $[m]$	position of the oscillator's tip at a given set of states	
	Identified Parameters	
C $[s \cdot m^{-4}]$	constant relating the deflection of the tip to the rotation velocity; given by Eq. 3	1.4×10^5
T $[s]$	time constant of the first order lag given by Eq. 3, 4	$0.02T_c$
m $[kg]$	mass of the second-order system given by Eq. 5	3.4×10^{-3}
b $[kg \cdot s^{-1}]$	damping coefficient of the second-order system given by Eq. 5	0.22
k $[N \cdot m^{-1}]$	spring stiffness of the second-order system given by Eq. 5	3.54

divided by the amplitude of oscillation, A. The angular velocities are divided by the nominal speed, ω_0. We represent the normalized parameters in the equations with the superscript notation '*'.

The material of the oscillators is flexible in order to allow bending to take place as a result of the applied viscous forces. In the experiment, the viscous forces acting on the oscillator induce dynamic deflection, γ_t, at the tip. The magnitude of that deflection is always small enough compared to the length; $\gamma_t \leq 0.05l$. By neglecting the shear and torsion stresses on the flexible flaplet, it can be modelled as a simple beam that experiences bending deflections while rotating.

In order to obtain the position of the tip as a function of time, we present the following set of differential equations. The description of the model parameters are given in Table 1. A references to the corresponding equations in appendix A is provided in bold font after each equation.

$$T\dot{\gamma}_o^* = -Cl^5\omega - \gamma_o^* \qquad \textbf{(\textit{Eq}. 16, 18)} \quad (3)$$

$$T\dot{\gamma}_{r,l}^* = u_{r,l} - \gamma_{r,l}^* \qquad \textbf{(\textit{Eq}. 17, 18)} \quad (4)$$

$$u_{r,l} = \begin{cases} 0.013d_{r,l} & r_{r,l}^* > 1 \\ d_{r,l}(-0.082r_{r,l}^* + 0.095) & r_{r,l}^* \leq 1 \end{cases}$$

$$m\ddot{\gamma}_t^* = k\left(\gamma_o^* + \gamma_r^* + \gamma_l^*\right) - b\dot{\gamma}_t^* - k\gamma_t^* \quad \textbf{(\textit{Eq}. 19)} \quad (5)$$

$$y^* = \frac{l}{A}\theta + \gamma_t^* \qquad (6)$$

4.2. State-Space Model

The above illustrated mathematical equations are gathered into a MISO state-space model that fully describes the dynamics of each oscillator. The model is given in the state space standard form as described by equations 7, 8. Since all equations are dimensionless, we then represent the normalized parameters in the state-space model without the superscript notation '*'.

$$\begin{bmatrix} \dot{\theta} \\ \dot{\gamma}_o \\ \dot{\gamma}_r \\ \dot{\gamma}_l \\ \dot{\gamma}_t \\ \ddot{\gamma}_t \end{bmatrix} = \begin{bmatrix} 0 & 0 & 0 & 0 & 0 & 0 \\ 0 & \frac{-1}{T} & 0 & 0 & 0 & 0 \\ 0 & 0 & \frac{-1}{T} & 0 & 0 & 0 \\ 0 & 0 & 0 & \frac{-1}{T} & 0 & 0 \\ 0 & 0 & 0 & 0 & 0 & 1 \\ 0 & \frac{k}{m} & \frac{k}{m} & \frac{k}{m} & \frac{-k}{m} & \frac{-b}{m} \end{bmatrix} \begin{bmatrix} \theta \\ \gamma_o \\ \gamma_r \\ \gamma_l \\ \gamma_t \\ \dot{\gamma}_t \end{bmatrix} + \begin{bmatrix} \omega_0 & 0 & 0 \\ -Cl^5 & 0 & 0 \\ 0 & \frac{1}{T} & 0 \\ 0 & 0 & \frac{1}{T} \\ 0 & 0 & 0 \\ 0 & 0 & 0 \end{bmatrix} \begin{bmatrix} \omega \\ u_r \\ u_l \end{bmatrix} \qquad (7)$$

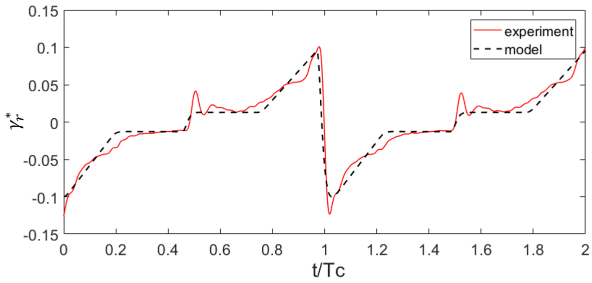

Figure 6: Normalized deflection of a still flaplet's tip due to the oscillation of its right neighbour during two successive beat cycles . the distance r between the two neighbouring tips varies in the domain $0 < r < 2A$ during a beat cycle.

$$y = \begin{bmatrix} \frac{l}{A} & 0 & 0 & 0 & 1 & 0 \end{bmatrix} \begin{bmatrix} \theta \\ \gamma_o \\ \gamma_r \\ \gamma_l \\ \gamma_t \\ \dot{\gamma}_t \end{bmatrix} \tag{8}$$

In Fig. 6, we present a comparison between the experiment and the model results of the deflection of a flaplet's tip due to the oscillation of its neighbour. The plot demonstrates the ability of the model to fairly capture the dynamic interaction between the neighbouring flaplets during the different phases of the beat cycle. Although minor deviation between the two responses can be observed, we assume that it does not affect the resulted variation of the beat cycle period during the transition from a chaotic to a coordinated beating pattern as illustrated in the next section.

5. Results and Analysis

The system is configured with the same setup as in the physical experiment in order to test the spontaneous emergence of synchronization among the oscillators and compare the results of both the model and the experiment. The synchronization is considered to start when the oscillators start to beat with the same frequency while keeping a certain phase shift between each other forming a metachronal wave. The experimental control loop algorithm described in section 3.2 is applied to the model as well. After investigating the emergence of hydrodynamic synchronization among the flaplets, the internal states of the system are analysed to better understand the synchronization effects.

5.1. Hydrodynamic Synchronization

Starting from random initial angular positions, 32 oscillators are brought together and allowed to interact by the help of their modelled bending deflections due to the surrounding viscous forces. The system as a unit could clearly show the emergence of metachronal coordination. Fig. 7 shows a colour representation of the position trajectories of individual oscillator tips as a function of the number of beat cycles. A straight uni-coloured line in the figure indicates a uniform inter-phase relationship throughout the system and hence metachronal coordination. The model has been rendered several times with different random initial positions. At each time, the system has eventually come into a synchronized state at which the phase slopes throughout the whole system remain the same. For different initial conditions, the emergence is found to choose between two steady-state phase slopes with the same slope magnitude but opposite directions. In other words, the uni-coloured lines at the steady state make an angle with the direction of time increase that can take the two values; α and $(180-\alpha)$. We believe that the dominating direction depends on the initial conditions and decides the direction of the swimming forces build up (discussed in the next section). Sometimes, either the very first or the very last oscillator at the edges appears to slightly lag the others during the synchronized state until it gradually joins the synchronization after a long term. As the edged oscillator, the cross-talk with its neighbours takes place on one side only and therefore it can be less sensitive to the viscous coupling.

The spontaneous synchronization could also be witnessed in several experiments of five oscillators while beating inside the glycerine fluid. Starting from different phase shifts between each couple of neighbours, the system has come into synchronization after 15 cycles. Fig. 8 shows a comparison between the emerged synchronization for five oscillators in the model (top) and in the experiment (bottom). As the oscillator moves inside the viscous fluid, it interacts with its neighbours in the from of bending. This results in time-variant velocities of the tips and phase relationships among the neighbouring oscillators. This behaviour lasts until the synchronization is reached when each oscillator maintains a certain phase lag with its neighbour that is constant among the beating system. The solid lines in the figure show a constant phase slope that indicates the start of synchronization in both cases. The dash lines that overlay the position trajectories are parallel to the synchronization lines. They show the different phase relationships between the adjacent oscillators at the start of beating and during the evolution of synchronization.

5.2. Net Propulsion Force

In this section, we investigate the ability of the mechanism to generate a net propulsion force from the action of the group of beating flaplets. The modelled forces acting on each oscillator are extracted from the system's internal states during the run-time such that:

$$f_m(t) = k\gamma = k\left(\gamma_r + \gamma_l + \gamma_o\right)$$

The force that act on a single oscillator is dependent on the phase relationship of the neighbours and takes the form of a quasi-harmonic function. In order to represent the effective swimming force, a cyclic average of the harmonic force signals as a function of time is calculated. The total effective swimming forces, F_t, is then represented as the summation

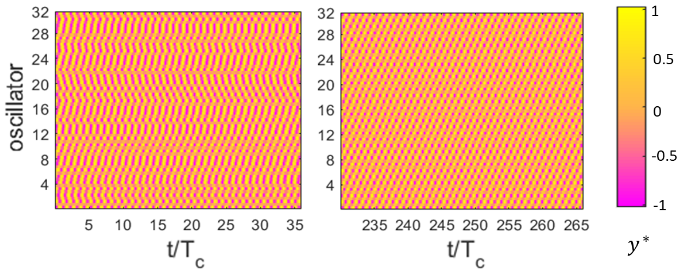

Figure 7: Position trajectories of 32 oscillators' tips in the modelled viscous environment. The randomness in the phase relationship is shown as curvy lines at the start of the beating (left). The emerged synchronization is shown as straight (constant slope) lines after 225 cycles from the start of beating (right)

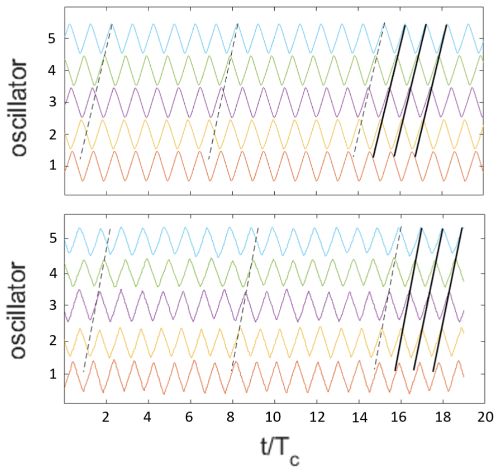

Figure 8: Evolution of synchronization in a row of five flexible oscillators in the model (top) and in the experiment (bottom). The different colours indicate different oscillators. The solid lines indicates a constant phase slope among four neighbouring oscillators and the dash lines are parallel to the solid ones and show the deviations from coordination at the early stages

of the single forces for all the oscillators in the system.

$$f_{av}(n) = \frac{1}{T_c}\int_{(n-1)T_c}^{nT_c} f_m(t)dt, \quad n \in \{1..300\}$$
$$F_t(n) = \sum_{i=1}^{N} f^{i}_{av}(n) \tag{9}$$

where N is the total number of oscillators rendered in the model and i is the oscillator index.

We found that effective swimming starts to emerge when the damping of the system is sufficiently high. This is implemented in the model by slightly increasing the damping of the flaplet's dynamic model. It can be also realized in the experiment by selecting a material of a lower Young's Modulus or a liquid of a higher viscosity.

Fig. 9 shows the temporal evolution of the normalized total forces, F_t/N, acting on a swimmer model of 32 and 16 oscillators at a high damping; $b = 0.5$. The resulted synchronization is found to build up in the direction of the increase of swimming effective forces and hence increasing the efficiency of propulsion. It is observed that even the undetectable small phase variations during the synchronized state (after reaching the straight slope lines in the position trajectories) result in a noticeable gain in the total effective forces. The periods after synchronization lines appear in the two models are highlighted in Fig. 9 by the blue- and red-shaded areas. Notice that the force gain, that is bounded by the dash lines in the figure, takes place in during these shaded periods.

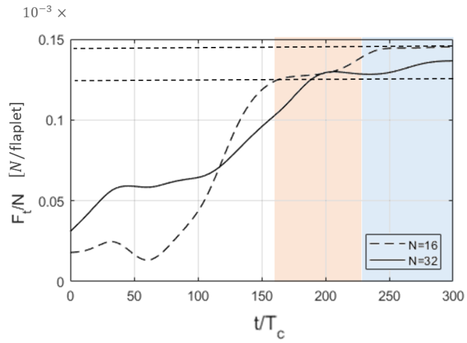

Figure 9: Evolution of the net propulsion force that arises due to the emerged synchronization at $b = 0.5$. The presented results are for 32- and 16-oscillator models respectively. The shaded areas represent the period after the synchronization lines (constant slope lines) are witnessed in the tips' position trajectories (red for $N = 16$ and blue for $N = 32$). The blue area is shown on top of the red area which also covers the part beneath it. The dash lines bounds the growth in the effective forces due to barely noticeable deviations in the phase slopes during the coordinated state

An interesting observation form the force response analysis is the stair-wise increase in the force build-up during the emergence of coordination. During the early stages, until approximately 50% of the settling time, the synchronization build-up is partial and separate segments of synchronized 3 to 4 neighbouring oscillators are formed. However, this is not reflected as a global increase of the effective swimming forces. The reason is that there are counteracting segments that are synchronized in opposite directions (slope angles of α and $180 - \alpha$) and therefore, the net propulsion force is not rising. After this period, a global tendency towards the final synchronization direction starts to emerge and the effect of this tendency is then clearly witnessed as an effective force build-up. The resulted net propulsion force is almost proportional to the number of flaplets in the system.

5.3. Stability of the Synchronization

Since the main goal of the model is to prove the emergence of both synchronization and propulsion, we choose the total effective force, $F_t(n)$ defined in equation 9 to study its long-term behaviour using the Lyapunov criterion. For a system of 32 oscillators we select $F_t(300)$ as the position of rest, $F_t(e)$. After computing $F_t(n)$ over a long period

($n = 10^3$), we find that;

$$\forall n > 280 \;\; \exists \epsilon < 0.01 F_t(e) \;\; [||F_t(n) - F_t(e)|| < \epsilon]$$

This means that starting from any position close enough to $F_t(e)$, the value of $F_t(n)$ remains close enough to $F_t(e)$ and within a range which does not exceed 1% of its value. Upon this analysis the synchronized system of 32 oscillator is Lyapunov stable.

A strong correlation could also be noticed between the initial conditions and the settling time the system takes until the position of rest is reached. In a robotic swimmer application, it is recommended to include a supervisory controller that can use the real-time model for state forecasting (as a state observer) and impose a set of initial conditions that would minimize the settling time. That said, we believe that even the maximum settling periods reported do not represent a problem in case of a micro-swimmer application. The smaller the size scale of the swimmer body and the inter-spacings is, the higher the beating frequency of oscillations that would keep a low Reynolds number. In recently reported micro-swimmer studies, the beating frequency reaches up to 60 Hz [29]. This frequency boost would result in a faster emergence of the required propulsion forces.

6. 2D Flow Visualization

In this section, we experimentally test the system capability to generate a coherent directed transport at the surface of the oscillators during metachronal coordination. In order to visualize the flow near the flaplet's surface, a Particle-Image-Velocimetry (PIV) measurement is prepared. Due to optical obstruction, the flow measurement cannot be carried out simultaneously while running the vision-based control loop. Therefore, an open-loop control algorithm is implemented to drive the five motors at a predefined amplitude, frequency and phase phase difference between each adjacent couple of motors. We define a general oscillatory profile of the motors as a triangle-wave form of θ which is described as a function of time t in the following equation:

$$\theta(t) = \frac{4A_\theta}{T_c}\left(t - \frac{T_c}{2}\left\lfloor \frac{2t}{T_c} + \frac{1}{2} \right\rfloor\right)(-1)^{\left\lfloor \frac{2t}{T_c} + \frac{1}{2} \right\rfloor} \tag{10}$$

where the symbol $\lfloor i \rfloor$ is the floor function of the number i and A_θ is the amplitude of the angular position of the motors. The trajectory of the n^{th} motor's rotation follows the profile prescribed by:

$$\theta_n(t) = \theta(t - jT_c(n-1)), \; n \in \{1..5\}, \; j \simeq 0.2 \tag{11}$$

where n is the motor index with the motors ordered from left to right and j is the cyclic ratio which quantifies the metachronal-wave phase shift among the oscillators as a factor of the beat cycle T_c.

The control algorithm is implemented in an NI cRio-9074 control unit (National Instruments, Austin, USA) using the LabVIEW FPGA software suite. Fig. 10 shows the experimental setup which is prepared in order to perform the PIV measurements for visualizing the flow around the beating flaplets. A Phantom Miro 310/311 Ametek camera is used to record the image of the flow around the flaplets. Fluorescent tracer-particles (50 μm in radius) are mixed with the glycerine liquid inside the flaplets' chamber. A continuous wave argon-ion laser beam (Raypower 5000, 5 W power at $\lambda = 532$ nm, Dantec Dynamics) is expanded to a light-sheet and used to illuminate the flow in the vertical (X-Y) plane along the centre of the flaplets. The light scattered by the particles is then captured and recorded in a synchronized mode, where the camera is set to capture a single frame per each beating cycle at the same phase (phase-locked imaging of the oscillators). Consequently, displaying the successive frames provides a visualization of the net cyclic transport of the particles.

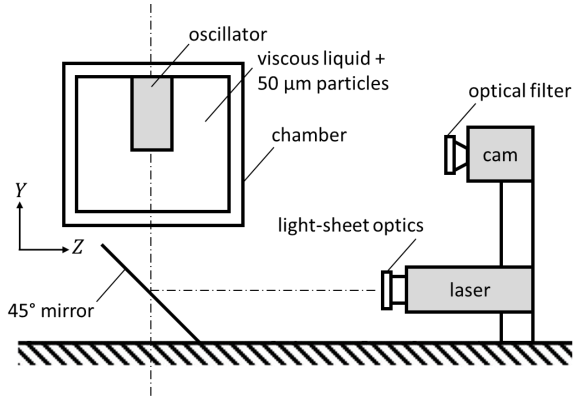

Figure 10: Schematic of the experimental setup for the Particle Image Velocimetry measurements. A vertical laser light-sheet parallel to the X-Y plane and passing through the centre of the flaplets is used along with the shown camera configuration to record the 2D flow field around the oscillators while beating in metachronal coordination

The metachronal wave form is set to match the wave that spontaneously emerged during the closed loop experiment which is reported here [20] in detail. A total of 105 particle images are recorded by the camera in a period of approximately 6 minutes. Fig. 11 shows the pathlines followed by the fluorescent particles while each oscillator is following the wave form prescribed by equation 11. The pathlines show a coherent structure of the flow below the flaplets which suggests that the flow at the vertical X-Y plane that passes through the centre of the flaplets can be considered steady in the present configuration. The figure shows smaller vortex structures below the flaplets' surface which arise due to the fact that the flaplets are close to the bottom wall while the chamber is closed.

In order to measure the velocity field of the flow, 2D cross-correlation of the successive frames of the particles is performed. The resulting time-averaged vector map of the velocity field of the 2D flow around the oscillators is shown in Fig. 12. Since the flow below the flaplets is mostly horizontal, we overlaid the vector map with the colour map of the horizontal component of the velocity u. As the graph

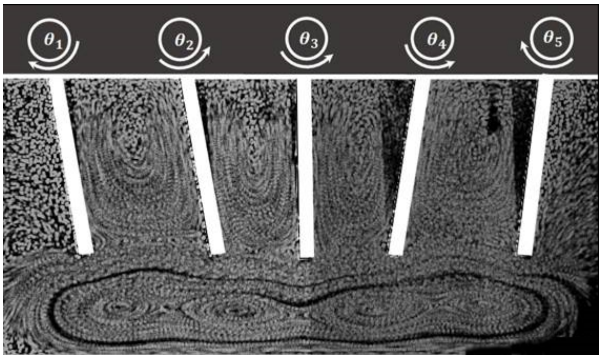

Figure 11: The pathlines of the tracer particles in the glycerine fluid as the flaplets follow the metachronal wave pattern prescribed by equation 11. The image is acquired by overlaying the frame of the flaplets with 5 phase-locked particle images that are recorded with a frame rate equal to the frequency of the flaplets' oscillatory motion. The direction of the flaplet oscillation at the instance of recording is shown by the white arrows

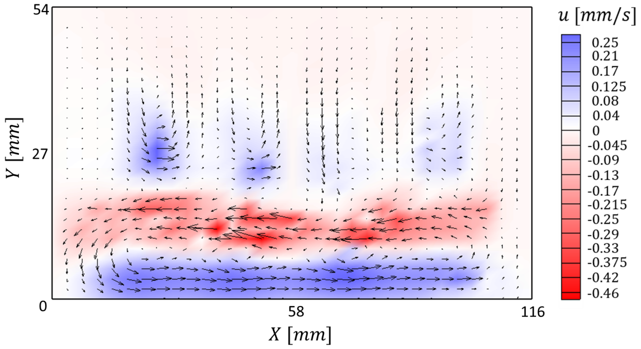

Figure 12: Time-averaged vector map of the velocity field in a vertical plane around the oscillators while beating in the metachronal coordination prescribed by equation 11. The color map overlaid with the graph represents the magnitude and direction of u in mm/s (the X component of the velocity vectors)

shows, the flow near the flaplets' surface is roughly coherent and directed to the left which shows a clear net pumping effect (steady streaming) of the metachronal wave. Since the flaplets are still, this transport can be a directional measure of the net cyclic force acting on the flaplets in the X direction.

In the lower part of the flow field near the bottom wall of the chamber, the fluid is moving to the right direction; opposite to the flow at the flaplets' tips. This is a consequence of the conservation of mass in the closed chamber. Adding horizontal fluid flow in the horizontal layer at the tips in an otherwise quiescent environment must be counter-balanced by the generation of another horizontal layer of flow in the opposite direction. Between the two layers, the fluid shear is forming the vortices known as the cat's eye vortices that can be seen in Fig. 11.

7. Conclusion

For low-Reynolds propulsion, we developed a model of a flat-plate swimmer that consists of rectangular shape-symmetric flexible oscillators. Each oscillator was modelled as a cantilever beam of a rectangular cross section, that can experience small deflections depending on its material and the surrounding viscous forces. The control of a single degree of freedom per each oscillator (the angle of rotation θ) was used to bound the individual oscillations to a certain amplitude. The viscous interaction forces among the oscillators and the surrounding fluid were modelled in form of induced bending deflections at each tip. This resulted in tip trajectories that slightly deviated from the position prescribed by the driving motor angles. This deviation allowed for the cross-talk to take place throughout the system which is necessary for the emergence of spontaneous coordination. The control algorithm was based on the geometric clutch hypothesis that illustrates the geometrical limits of the oscillations in biological ciliary micro-swimmers.

Starting from random phase relationships, we could show the emergence of both the hydrodynamic synchronization and the propulsion for this design of swimmers. The results of synchronization were compared to the produced data of a five-oscillator experiment in a viscous environment. The comparison confirmed similar coordination patterns and time scales.

The internal states of the model were then combined to represent the effective global force that acts on the swimmer due to its body-fluid interaction. The temporal evolution of the global force showed the emergence of a swimming action as the system damping goes higher. After reaching the synchronized state, the effective force still showed a remarkable increase towards its maximum value due to hardly detected variations in the oscillators' relative phases. The magnitude of the net propulsion force was found to be a linear function of the number of oscillators in the system.

The simplicity of the proposed model's design allows for its application in different scales and environments. The flexible oscillator is a rotating flat plate attached to a rotary motor. The deflection induced at the oscillator tip, due to the surrounding viscous forces and the neighbouring oscillators, is isotropic. Several actuation mechanisms can be used to drive the rotary motion. The linearity of the model and the observability of its internal states nominate it for real-time observer applications. Moreover, the model can be utilized for the forecasting of the settling time and the direction of the resulting forces due to a set of initial conditions.

Furthermore, the stability of the emerged synchronization in the introduced model was analysed. To begin with, the synchronization was defined as a constant phase difference between each neighbouring couple of oscillators in the beating system. This state was recognized by a constant slope (straight uni-coloured lines) in the position trajectories plots. It was observed that once the system formed this coordinated pattern, partially or globally, it kept this state from there on. However, after analysing the emerged swimming force, we found that it still tended to increase up to its maximum value even after the first synchronization lines appeared. Accordingly, we applied the Lyapunov stability criterion on the resulted swimming forces. The long-term study showed that the system is Lyapunov stable as the value of the induced force, starting from any position close to its rest position, remained close enough to that steady-state value for the rest of the study period.

At the end, we experimentally measured the 2D velocity field of the flow around the oscillators while beating in metachronal coordination ($j \simeq 0.2$) using Particle Image Velocimetry. The results showed a uni-directional steady-streaming transport of the fluid at the surface of the oscillators which can be translated into an effective propulsion force if the oscillators were attached to a body that is free to move.

A. Derivation of the Mathematical Model

At very low Reynolds numbers $Re \ll 1$, analytical expressions that describe the motion of slender bodies in Stokes flow can be used to mathematically represent interacting oscillatory systems. The reader is referred to the study here [30] which examines the hydrodynamic behaviour of a slender ribbon in the Stokes flow, and the study presented in [6] which investigates the unsteady Stokes flow around oscillatory slender bodies. The analysis performed there can be of interest in modelling the hydrodynamic interaction among oscillating elements in that Reynolds regime. On the other hand, at a Reynolds number close to unity, the effect of inertial forces cannot be completely neglected. Therefore the Stokes flow expressions are less relevant in our present study where $\mathrm{Re} \in [0.1, 1]$.

The model described herein is derived on the basis of a dynamic system of which the steady-state variables are identified from theory and the experiments. This model is then rendered in Matlab Simulink to simulate the time-varying behavior of the system under given initial conditions (angle θ at time $t = 0$). The model assumes a linear superposition of the bending contributions (self-oscillations and viscous coupling) and a first order response for their build-up. The dynamic behaviour of each oscillator is modelled as a second order response of a one-sided clamped Euler-Bernoulli beam. The different contributions to the mathematical model are given below.

Steady-State modelling

The steady-state of the cantilever beam is represented by the total deflection of the tip $\gamma(l)$. Fig. 13 shows the model beam and its curvature parameters in response to an applied load. The radius of curvature of the deflected beam is inversely proportional to the bending moment, M, applied on it [5]. By relating the beam deflection to the radius of curvature, we end up with the differential equation of static beam deflection (Eq. 12).

$$\frac{d^2\gamma(t\to\infty)}{dx^2} = \frac{M(x)}{EI}, \quad \frac{d^2M}{dx^2} = \frac{dH_s}{dx} = q(x) \quad (12)$$

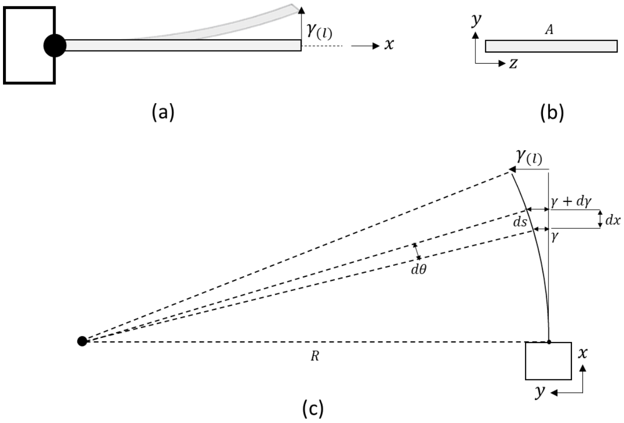

Figure 13: (a,b) Schematic view of the oscillator model as a simple beam (c) the curvature of deflection and strain parameters in the x-y plane. The deflection of the oscillator is magnified in the figures for better visibility. The actual deflection does not exceed 5% of the total length. The coordinate system (x,y,z) introduced here is attached to the oscillator and inherits its orientation while the global coordinate system (X,Y,Z) is presented in Fig. 10

where $\gamma(t \to \infty)$ is the steady state deflection, EI is the flexural rigidity of the oscillator, H_s is the shear load and $q(x)$ is the distributed load per unit length acting normal to the x-z face of the flaplet. Equation 12 can be solved to find an expression of the steady-state deflection of the beam's tip for a given load profile. The latter is composed of two contributions, first the load due to the drag-forces acting on the flap while rotating in the viscous liquid and secondly the effect of the neighbouring oscillators on the pressure and velocity due to viscous coupling. Given that the beam differential equation, Eq. 12, is linear, the principle of superposition holds. It means that the steady-state total deflection of a beam can be represented as the summation of the individual deflection amounts of multiple decoupled forces. Eq. 13 describes the total steady state deflection of a flaplet, γ as the sum of γ_o^* due to its own rotation in the viscous medium and $\gamma_{r,l}^*$ due to its interaction with the right and left neighbouring oscillator.

$$\gamma^*(t\to\infty) = \gamma_o^*(t\to\infty) + \sum_{i\in\{l,r\}} \gamma_i^*(t\to\infty) \quad (13)$$

Force Contribution Due to Rotation in a Still Fluid

Considering the case when the flaplet is freely rotating inside the glycerine liquid. Note that the background fluid in this case is considered still, therefore $v_r = \omega x$ when the flaplet is rotating with an angular speed of ω. The load profile on the oscillator at $\mathrm{Re} \in [0.1, 1]$ can be derived from the drag coefficient of a flat rectangular plate , which is experimentally investigated in [27] for Re< 2 and found to be

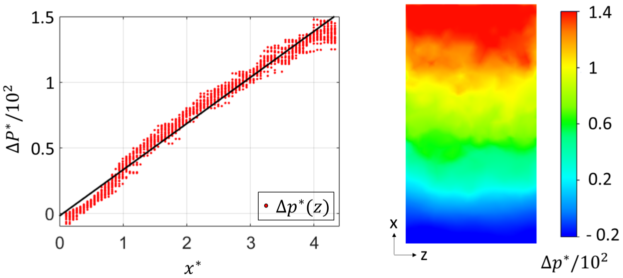

Figure 14: CFD model results of the normalized pressure difference between the x-z faces of a flaplet that rotates inside the viscous medium at a Reynold number of Re≃0.2

inversely proportional to the Reynolds number, Eq. 14 [27]:

$$C_d = \frac{\kappa}{Re} = \frac{\kappa\mu}{\rho v_r l} \rightarrow q(x) = \frac{1}{2}\rho w C_d {v_r}^2 \qquad (14)$$

$$q(x) = -R_\perp v_r$$

where ρ is the fluid density and v_r is the velocity of the body relative to the background. Similar to the resistance definition in Stokes flow, we combine the factors leading the relative velocity in eq. 14 as the resistance drag coefficient $-R_\perp$ in direction normal to the surface and use it in the following analysis (the negative sign indicates that the direction of the drag force is opposite to the direction of the local relative speed). Eq 14 suggests that the load q(x) acting on the rotating plate at this regime is directly proportional to its speed $v_r = \omega x$ and therefore varies linearly along the flap $q(x) \propto x$.

In order to validate this assumption and to show that the load is constant along the span a CFD numerical model of the flaplet was generated inside the ANSYS Workbench multiphysics platform. The Finite Volume Fluent Solver was used to solve the Navier-Stokes equations and capture the pressure field on the flaplet while rotating at a Reynolds number of Re≃0.2. Fig. 14 shows the CFD results of the pressure field on the x-z face of the flaplet while rotating in the glycerine fluid. The dimensionless notations, p^* and $x*$ are used where $p^* = p/\rho(\omega l)^2$ and $x^* = x/A$.The figure shows a linear fit that fairly describes the load distribution along the flaplet's length.

Finally, the solution to eq 12 with the boundary conditions $H_s(0) = M(0) = \dot{\gamma}(0) = \gamma(0) = 0$ provides the magnitude of deflection at a distance x from the flaplet's root in the direction opposite to the local velocity at this point:

$$q(x) = -R_\perp v_r = -R_\perp \omega x$$

$$\gamma_o(x, t \rightarrow \infty) = \frac{R_\perp}{5!\ EI}\omega x^5$$

$$\gamma_o^*(x, t \rightarrow \infty) = -C\omega^* x^5, \quad C = \frac{\omega_0}{A}\frac{R_\perp}{5!\ EI} \qquad (15)$$

In order to evaluate the deflection magnitude for a given ω, the value of C is experimentally identified. Therefore, we record the tip deflection of a flaplet while rotating in glycerine with different speeds. Fig. 15 shows the relation between the normalized deflection at the tip and the different angular speeds. The linear fitting line provides the missing value given in Eq. 16. We only consider the deflection at the tip; $x = l$ in our model. Therefore, we will represent the deflection as a function of time only; $\gamma^*(l,t) = \gamma^*(t)$.

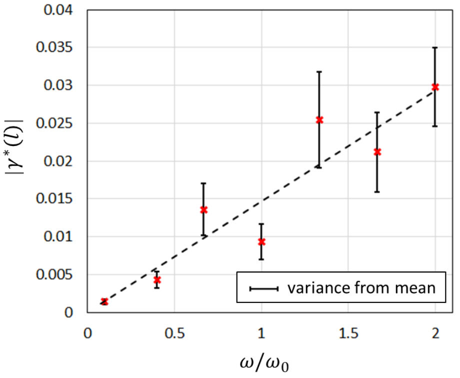

Figure 15: Normalized deflection magnitude of a rotating flaplet in glycerine as a function of its normalized angular speed. The bar lines indicates the deviation of the dynamic deflection from its mean during a single beat cycle

$$\gamma_o^*(t \rightarrow \infty) = -0.0145\omega^*, \quad C = 1.4 \times 10^5 \qquad (16)$$

Force Contribution Due to Viscous Interaction

The effect of viscous interaction on the flap bending depends on the distance r between the tips of two neighbouring flaplets. A further experiment was done, where we allow two neighbouring flaplets (one is rotating and the other is still; $\Delta\omega = \omega_0$) to interact in the viscous fluid and we measure the deflection at the tip of the still flaplet. Fig. 16 shows a plot of the normalized deflection of the tip, $\gamma^*(l)$, as a function of r^*. For simplification, we fit a linear function to the part of the curve where $\gamma^*(l) > 0.02$. We can then take $\delta_r^* \simeq 1$ beyond which the interaction is considered constant; $\gamma^*(l) = 0.013$ as highlighted on the plot. Since $r^* = 2$ is the maximum the distance between the neighbouring flaplets can get, we do not account for the domain $r^* > 2$. For the given configuration in the experiment, δ is the boundary limit beyond which the effect of an oscillator rotation on its neighbour deflection at the tip is almost constant.

As described in section 3.2, the variation of the phase relationships among the flaplets until they reach coordination is dependent on the deflection values at the their tips. Fig. 16 shows that the deflection of a still flaplet due to the rotation of its neighbour can reach up to 10% of the oscillation amplitude. This observation highlights the significance of the viscous interaction among the flaplets in the emergence of their self-assembly.

According to the experimental result shown in Fig. 16, we can approximate the bending interaction of a flaplet due to a rotating neighbour with the following definition:

$$\gamma_{r,l}^*(t \rightarrow \infty) = \begin{cases} 0.013 d_{r,l} & r_{r,l}^* > 1 \\ d_{r,l}(-0.082 r_{r,l}^* + 0.095) & r_{r,l}^* \leq 1 \end{cases}$$

$$d_{r,l} = \frac{\Delta\omega}{\omega_0} \qquad (17)$$

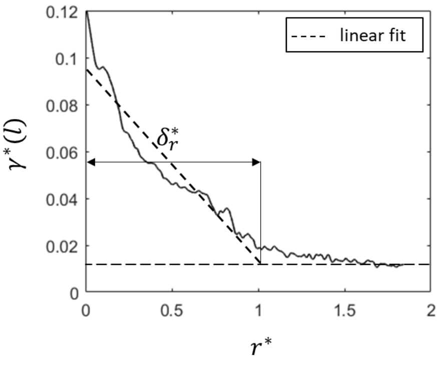

Figure 16: Normalized deflection of a still flaplet due to the rotation of its neighbour as a function of the normalized distance between their tips. The ramp dashed line is a linear fit for the deflection values that are greater than 2% of the oscillation amplitude. From there the deflection is considered constant.

in which $d_{r,l}$ is a dimensionless factor that accounts for the direction of the rotational speed of the right/left neighbour, $\omega_{r,l}$, relative to the flaplet's self rotation, ω. This linear approximation for the two different domains allows for the use of the principle of superposition.

Dynamics Modelling

The system dynamics can be divided into two time-invariant dynamic systems that describe the oscillator as well as its surrounding viscous medium. In this section the two models are deduced and identified using results from the experiments.

Fluid Dynamics

The unsteady behaviour of the fluidic forces on the bending is represented by a first-order system as the system is investigated at low Re-number and dominated by viscous diffusion. This considers the time-constant of the build-up of the deflection forces induced by the rotation of the flaplet in the viscous medium and its interaction with the neighbouring oscillators. This leads to a transient response of the deflection (γ) :

$$\gamma^*(t) = \gamma^*(t \to \infty)(1 - e^{\frac{t}{T}}) \tag{18}$$

The time constant, T, is tuned to best match the experimental response described in the section 4.2 and is found to be at least one order of magnitude lower than the characteristic cycle period.

Oscillator Dynamics

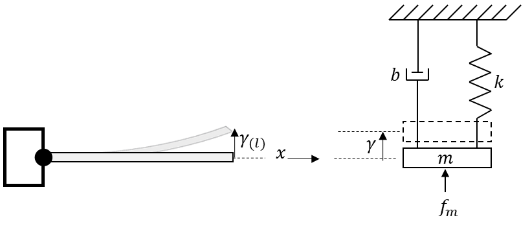

Figure 17: The model of the flexible flat-plate oscillator as a mass-spring-damper system

The proposed cantilever beam model, shown in Fig. 17, is a second order dynamic system which is analogous to a mass-spring-damper system. This representation is well established and can be derived from the Euler-Bernoulli beam theory and used as a reduced order model of the oscillator [42, 4]. The final response of the deflection of the oscillator tip can be represented by:

$$\gamma_t^*(t) = \gamma^*\left[1 - \left(\frac{\lambda_2}{\lambda_2 - \lambda_1}e^{\lambda_1 t} + \frac{\lambda_1}{\lambda_1 - \lambda_2}e^{\lambda_2 t}\right)\right] \tag{19}$$

$$\lambda_1, \lambda_2 = -\zeta\omega_n \pm \omega_n\sqrt{\zeta^2 - 1}$$

In order to identify the value of ω_n at low Reynolds numbers, we refer to the first mode of vibration of the Euler-Bernoulli beam model [26].

$$\omega_n = 3.5161\sqrt{\frac{EI}{m_t l^3}}$$

in which m_t is the total inertia of the oscillating mechanism.

The oscillator while moving is forcing a part of the liquid mass to move along with it. This leads to an increase in the total effective inertia and consequently a lower output frequency [48]. The above relation becomes:

$$\omega_n = \frac{3.5161}{l^2}\sqrt{\frac{EI}{\rho_o bh + \mu_a}} \tag{20}$$

where ρ_o is the oscillator density, b is its width, h is its thickness and μ_a is the added mass per unit length.

According to [31, 25], the added mass density of a rectangular plate due to the presence of the viscous fluid can be approximated by:

$$\mu_a = 0.6\rho_f l^{0.5} b^{1.5}$$

where ρ_f is the liquid density. By substituting the value of μ_a in equation 20, we get $\omega_n = 32.3$.

We then experimentally investigate the response of the flexible oscillator due to an initial imposed small deflection at its tip, $\gamma(0) = 0.05l$. Using a high-speed camera, we could capture the response of the oscillator in the viscous fluid as shown in Fig. 18. We can then estimate the period that the tip takes to reach within a range of 5% of $\gamma(0)$ around its position of rest. This period represents the settling time of the damped system, $T_{95\%} = 0.026T_c$, where T_c is the cycle period.

The damping coefficient, ζ, is then tuned to achieve the same settling time in the proposed second order model. The optimum value of ζ is then found to be $\zeta = 1.04$.

Accordingly, the values of k, m and b can be calculated assuming that the spring stiffness $k = 3EI/L^3$ [10]

$$2\zeta\omega_n = \frac{b}{m_{eff}}, \quad \omega_n = \sqrt{\frac{k}{m_{eff}}}$$

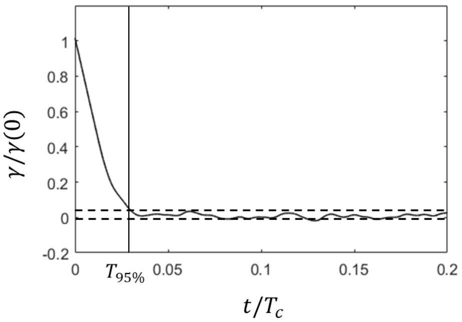

Figure 18: Measured response of the oscillator's tip in the glycerine liquid due to an initial imposed deflection; $\gamma(0)$

$$m_{eff} = 3.4 * 10^{-3}, \quad b = 0.22, \quad k = 3.54$$
$$f_m = k\gamma$$

Acknowledgment

The authors would like to thank the Deutsche Forschungsgemeinschaft (DFG) for funding this research project under reference number BR 1491/30-1. The position of Christoph H. Bruecker is co-funded as the BAE SYSTEMS Sir Richard Olver Chair and the Royal Academy of Engineering Chair (grant RCSRF1617/4/11) which is gratefully acknowledged.

References

[1] Abbott, J.J., Peyer, K.E., Lagomarsino, M.C., Zhang, L., Dong, L., Kaliakatsos, I.K., Nelson, B.J., 2009. How should microrobots swim? The international journal of Robotics Research 28, 1434–1447.

[2] Allan, R.A., Elgar, M.A., Capon, R.J., 1996. Exploitation of an ant chemical alarm signal by the zodariid spider habronestes bradleyi walckenaer. Proceedings of the Royal Society of London. Series B: Biological Sciences 263, 69–73.

[3] Ball, P., 2013. Material witness: When water doesn't wet. Nature materials 12, 289.

[4] Banks, H.T., Inman, D., 1991. On damping mechanisms in beams. Journal of applied mechanics 58, 716–723.

[5] Bansal, R., 2010. A textbook of strength of materials. Laxmi Publications.

[6] Barta, E., 2011. Motion of slender bodies in unsteady stokes flow. Journal of fluid mechanics 688, 66–87.

[7] Batchelor, C.K., Batchelor, G., 2000. An introduction to fluid dynamics. Cambridge university press.

[8] Becker, L.E., Koehler, S.A., Stone, H.A., 2003. On self-propulsion of micro-machines at low reynolds number: Purcell's three-link swimmer. Journal of fluid mechanics 490, 15–35.

[9] Beckers, R., Goss, S., Deneubourg, J.L., Pasteels, J.M., 1989. Colony size, communication and ant foraging strategy. Psyche: A Journal of Entomology 96, 239–256.

[10] Bellon, L., 2008. Thermal noise of microcantilevers in viscous fluids. Journal of Applied Physics 104, 104906.

[11] Blake, J.R., Sleigh, M.A., 1974. Mechanics of ciliary locomotion. Biological Reviews 49, 85–125.

[12] Brumley, D.R., Wan, K.Y., Polin, M., Goldstein, R.E., 2014. Flagellar synchronization through direct hydrodynamic interactions. Elife 3, e02750.

[13] Bruot, N., Cicuta, P., 2016. Realizing the physics of motile cilia synchronization with driven colloids. Annual Review of Condensed Matter Physics 7, 323–348.

[14] Cho, S., et al., 2014. Mini and micro propulsion for medical swimmers. Micromachines 5, 97–113.

[15] De Langre, E., 2001. Fluides et solides. Editions Ecole Polytechnique.

[16] Di Leonardo, R., Búzás, A., Kelemen, L., Vizsnyiczai, G., Oroszi, L., Ormos, P., 2012. Hydrodynamic synchronization of light driven microrotors. Physical review letters 109, 034104.

[17] Dreyfus, R., Baudry, J., Stone, H.A., 2005. Purcell's "rotator": mechanical rotation at low reynolds number. The European Physical Journal B-Condensed Matter and Complex Systems 47, 161–164.

[18] Earl, D.J., Pooley, C., Ryder, J., Bredberg, I., Yeomans, J., 2007. Modeling microscopic swimmers at low reynolds number. The Journal of chemical physics 126, 02B603.

[19] Elgeti, J., Gompper, G., 2013. Emergence of metachronal waves in cilia arrays. Proceedings of the National Academy of Sciences 110, 4470–4475.

[20] Elshalakani, M., Brücker, C., 2018. Spontaneous synchronization of beating cilia: An experimental proof using vision-based control. Fluids 3, 30.

[21] Eshel, D., Priel, Z., 1987. Characterization of metachronal wave of beating cilia on frog's palate epithelium in tissue culture. The Journal of physiology 388, 1–8.

[22] Gao, W., Feng, X., Pei, A., Kane, C.R., Tam, R., Hennessy, C., Wang, J., 2013. Bioinspired helical microswimmers based on vascular plants. Nano letters 14, 305–310.

[23] Gauger, E.M., Downton, M.T., Stark, H., 2009. Fluid transport at low reynolds number with magnetically actuated artificial cilia. The European Physical Journal E 28, 231–242.

[24] Golestanian, R., Yeomans, J.M., Uchida, N., 2011. Hydrodynamic synchronization at low reynolds number. Soft Matter 7, 3074–3082.

[25] Greenspon, J.E., 1961. Vibrations of cross-stiffened and sandwich plates with application to underwater sound radiators. The Journal of the Acoustical Society of America 33, 1485–1497.

[26] Han, S.M., Benaroya, H., Wei, T., 1999. Dynamics of transversely vibrating beams using four engineering theories. Journal of Sound and vibration 225, 935–988.

[27] Jones, A.M., 1957. Drag coefficients for flat plates, spheres, and cylinders moving at low reynolds numbers in a viscous fluid .

[28] Kapral, R., 2008. Multiparticle collision dynamics: Simulation of complex systems on mesoscales. Advances in Chemical Physics 140, 89–146.

[29] Kim, S., Lee, S., Lee, J., Nelson, B.J., Zhang, L., Choi, H., 2016. Fabrication and manipulation of ciliary microrobots with non-reciprocal magnetic actuation. Scientific reports 6, 30713.

[30] Koens, L., Lauga, E., 2016. Slender-ribbon theory. Physics of Fluids 28, 013101.

[31] Korayem, M., Ebrahimi, N., Sotoudegan, M., 2011. Frequency response of atomic force microscopy microcantilevers oscillating in a viscous liquid: A comparison of various methods. Scientia Iranica 18, 1116–1125.

[32] Kotar, J., Leoni, M., Bassetti, B., Lagomarsino, M.C., Cicuta, P., 2010. Hydrodynamic synchronization of colloidal oscillators. Proceedings of the National Academy of Sciences 107, 7669–7673.

[33] Lindemann, C.B., 1994. A" geometric clutch" hypothesis to explain oscillations of the axoneme of cilia and flagella. Journal of theoretical biology 168, 175–189.

[34] Machemer, H., 1974. Ciliary activity and metachronism in protozoa. Cilia and Flagella , 199–286.

[35] Mason, R., Burdick, J., 1999. Propulsion and control of deformable bodies in an ideal fluid, in: Proceedings 1999 IEEE International Conference on Robotics and Automation (Cat. No. 99CH36288C), IEEE. pp. 773–780.

[36] Najafi, A., Golestanian, R., 2004. Simple swimmer at low reynolds number: Three linked spheres. Physical Review E 69, 062901.

[37] Niedermayer, T., Eckhardt, B., Lenz, P., 2008. Synchronization, phase locking, and metachronal wave formation in ciliary chains. Chaos: An Interdisciplinary Journal of Nonlinear Science 18, 037128.

[38] OpenCV, 2000-2019. URL: `https://opencv.org`. last accessed: 2019-08-13.

[39] Polmanteer, K.E., 1988. Silicone rubber, its development and technological progress. Rubber chemistry and technology 61, 470–502.

[40] Purcell, E.M., 1977. Life at low reynolds number. American journal of physics 45, 3–11.

[41] Putz, V.B., Yeomans, J.M., 2009. Hydrodynamic synchronisation of model microswimmers. Journal of Statistical Physics 137, 1001.

[42] Rao, S.S., 2007. Vibration of continuous systems. volume 464. Wiley Online Library.

[43] Ricci, N., 1990. The behaviour of ciliated protozoa. Animal behaviour 40, 1048–1069.

[44] Rockenbach, A., Mikulich, V., Brücker, C., Schnakenberg, U., 2015. Fluid transport via pneumatically actuated waves on a ciliated wall. Journal of Micromechanics and Microengineering 25, 125009.

[45] Shih, C., Litt, M., Khan, M., Wolf, D., 1977. Effect of nondialyzable solids concentration and viscoelasticity on ciliary transport of tracheal mucus. American Review of Respiratory Disease 115, 989–995.

[46] TAMM, S.L., 1973. Mechanisms of ciliary co-ordination in ctenophores. Journal of Experimental Biology 59, 231–245.

[47] Trouilloud, R., Tony, S.Y., Hosoi, A., Lauga, E., 2008. Soft swimming: Exploiting deformable interfaces for low reynolds number locomotion. Physical review letters 101, 048102.

[48] Vančura, C., Dufour, I., Heinrich, S.M., Josse, F., Hierlemann, A., 2008. Analysis of resonating microcantilevers operating in a viscous liquid environment. Sensors and Actuators A: Physical 141, 43–51.

[49] Vicider, C., Ohman, O., Elderstig, H., 1995. A pneumatically actuated micro valve with a silicone rubber membrane for integration with fluid-handling systems, in: Proceedings of the International Solid-State Sensors and Actuators Conference-TRANSDUCERS'95, IEEE. pp. 284–286.

[50] Xu, T., Hwang, G., Andreff, N., Régnier, S., 2014. Modeling and swimming property characterizations of scaled-up helical microswimmers. IEEE/ASME Transactions on Mechatronics 19, 1069–1079.

[51] Yang, Y., Elgeti, J., Gompper, G., 2008. Cooperation of sperm in two dimensions: synchronization, attraction, and aggregation through hydrodynamic interactions. Physical Review E 78, 061903.